

Chemistry

Intermolecular coupling enhanced thermopower in single-molecule diketopyrrolopyrrole junctions

Chao Fang^{1,#}, Renad Almughathawi^{2,6,#}, Qingqing Wu^{2,#}, Wenqiang Cao^{1,#}, Hang Chen^{1,#}, Songjun Hou², Yu Gu¹, Hewei Zhang¹, Yi Zhao¹, Jueting Zheng¹, Guopeng Li¹, Jia Shi¹, Junyang Liu^{1,4}, Bing-Wei Mao¹, Zitong Liu^{3,5,*}, Colin J. Lambert^{2,*} & Wenjing Hong^{1,4,5,*}

¹State Key Laboratory of Physical Chemistry of Solid Surfaces, College of Chemistry and Chemical Engineering, Xiamen University, Xiamen 361005, China;

²Department of Physics, Lancaster University, Lancaster LA1 4YB, UK;

³State Key Laboratory of Applied Organic Chemistry (SKLAOC), College of Chemistry and Chemical Engineering, Lanzhou University, Lanzhou 730000, China;

⁴Innovation Laboratory for Sciences and Technologies of Energy Materials of Fujian Province (IKKEM), Xiamen 361005, China;

⁵Beijing National Laboratory for Molecular Sciences, Beijing 100190, China;

⁶Department of Physics, Faculty of Science, Taibah University, Madinah, Saudi Arabia

#Contributed equally to this work.

*Corresponding authors (emails: liuzt@lzu.edu.cn (Zitong Liu); c.lambert@lancaster.ac.uk (Colin J. Lambert); whong@xmu.edu.cn (Wenjing Hong))

Received 15 May 2022; Revised 11 October 2022; Accepted 11 October 2022; Published online 28 December 2022

Abstract: Sorting out organic molecules with high thermopower is essential for understanding molecular thermoelectrics. The intermolecular coupling offers a unique chance to enhance the thermopower by tuning the bandgap structure of molecular devices, but the investigation of intermolecular coupling in bulk materials remains challenging. Herein, we investigated the thermopower of diketopyrrolopyrrole (DPP) cored single-molecule junctions with different coupling strengths by varying the packing density of the self-assembled monolayers (SAM) using a customized scanning tunneling microscope break junction (STM-BJ) technique. We found that the thermopower of DPP molecules could be enhanced up to one order of magnitude with increasing packing density, suggesting that the thermopower increases with larger neighboring intermolecular interactions. The combined density functional theory (DFT) calculations revealed that the closely-packed configuration brings stronger intermolecular coupling and then reduces the highest occupied molecular orbital (HOMO)-lowest unoccupied molecular orbital (LUMO) gap, leading to an enhanced thermopower. Our findings offer a new strategy for developing organic thermoelectric devices with high thermopower.

Keywords: single-molecule electronics, single-molecule junctions, thermopower, thermoelectric devices, intermolecular coupling

INTRODUCTION

Thermoelectric materials offer the opportunity for direct conversion of heat into electric energy via Seebeck effects [1–4], and the efficiency of thermoelectric devices can be evaluated through the dimensionless figure of merit $ZT = GS^2T/\kappa$, where G is the electrical conductance, S is the Seebeck coefficient, T is the temperature, and $\kappa = \kappa_{el} + \kappa_{ph}$ is the thermal conductance due to electrons (κ_{el}) and phonons (κ_{ph}) [5]. Compared with

inorganic thermoelectric materials, molecular thermoelectric materials exhibit lower thermal conductivity (κ_{ph}) and higher flexibility with tunable electronic structures [6–9], some pioneering theoretical works even suggested that molecular thermoelectric devices can reach the highest ZT value up to 5.9 [10]. However, the experimentally determined Seebeck coefficients of the molecule-scale thermoelectric materials are still much lower than theoretical predictions [11–13]. Strategies to enhance the Seebeck coefficient are crucial for developing high thermoelectric performance devices at the single-molecule scale.

To increase the ZT of the molecular devices [14], various strategies have been investigated to improve the thermopower, including varying molecular length of organic building blocks [11,15,16], changing connectivity of molecular cores [17–20], tuning molecule-electrode coupling [21], exploring different anchor groups [22] and substituent groups [23]. More importantly, theoretical advances revealed that the intermolecular interactions, such as π - π stacking, will enhance ZT by suppressing the phonon contribution to lowering the thermal conductance [12], suggesting that the intermolecular interactions are essential for the design of molecular devices with high ZT [24,25]. However, the role of intermolecular interactions in the thermopower of molecular devices has not yet been experimentally investigated, which is mainly due to the challenges in the control of intermolecular interactions at the single-molecule level. Previous studies have demonstrated that the π - π interaction between the porphyrins in the mixed self-assembled monolayers (SAMs) decreases with reducing the concentration of porphyrin during the assembling process [26], which offers the strategy to tune intermolecular couplings by varying packing density in the SAMs and explore how the presence of intermolecular coupling affects the thermoelectric properties from molecular level [27–29].

In this work, we investigated the Seebeck coefficient of diketopyrrolopyrrole (DPP) molecular junctions by varying the packing density of their SAMs. The three target DPPs of difuranyl-DPP (**F-DPP**), dithienyl-DPP (**T-DPP**), dithiazolyl-DPP (**Thia-DPP**) with *p*-methylthiobenzenes at both ends are shown in Figure 1A (see Figure S1 for synthesis information). To explore the effect of packing density on thermoelectric properties of the single-molecule junctions, we assembled the molecule on a gold surface through immersion in different solutions with different concentrations [30]. We found that the Seebeck coefficients of all DPPs increase with growing molecular packing density. Besides, density functional theory (DFT) based calculations revealed that stronger intermolecular coupling associated with higher packing densities generally reduces the energy gap and leads to an enhanced thermopower on DPP molecules.

RESULTS

A customized scanning tunneling microscope break junction (STM-BJ) instrument [31,32] was used to simultaneously measure the conductance and thermopower of the single-molecule junctions at room temperature (Figure 1B). A Peltier device mounted under the substrate was used as a heater to establish a stable temperature difference ($\Delta T = T_{\text{substrate}} - T_{\text{tip}}$) between the tip (at room temperature, ~ 298 K) and the substrate (heated) [11,33]. The thermopower measurement was performed for four temperature differences ($\Delta T = 0, 5, 10$ and 15 K). To obtain a statistical distribution of ΔV of an Au-Molecule-Au junction, we have collected more than 1000 consecutive data at each ΔT and selected those that sustained a molecular junction through the entire “hold” period (see Figure S2 for details of thermoelectric measurement process).

The typical individual thermovoltage traces and histograms are shown in Figure 1C for a single **F-DPP**

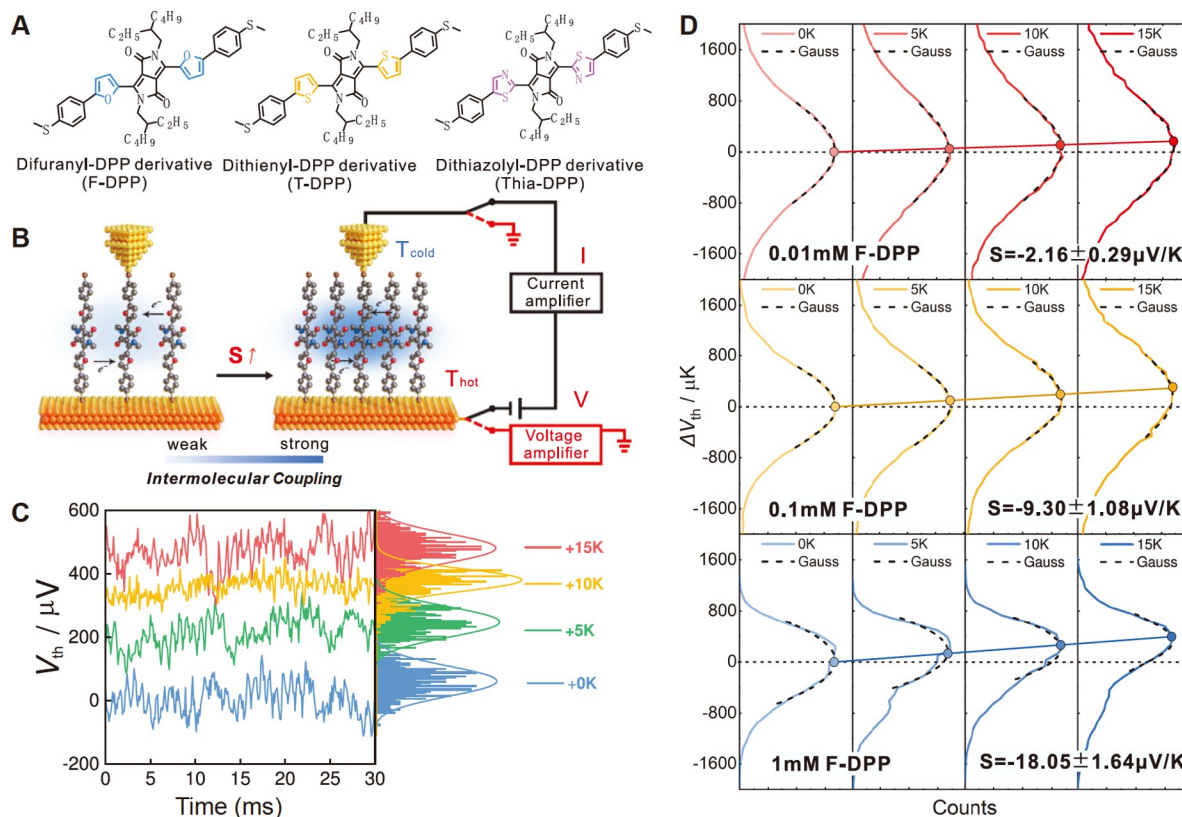


Figure 1 Schematic diagram of experimental setup and Seebeck coefficient measurement. (A) Molecular structures of DPP derivatives studied in this work. (B) Schematic of the experimental setup. Closely packed molecules enhance the Seebeck coefficient due to stronger intermolecular coupling. (C) Typical measured individual thermovoltage traces and histograms for single **F-DPP** molecule with 1 mmol/L immersion concentration at a series of ΔT (0, 5, 10, and 15 K). (D) Histograms of single **F-DPP** molecule thermoelectric voltage measurements with different immersion concentrations (0.01, 0.1, 1 mmol/L). Gaussian fits were plotted in a black dash curve. The horizontal black dash line indicates the baseline of thermoelectric voltage at $\Delta V_{th}=0$. The Seebeck coefficients were obtained from the thermovoltage as a function of ΔT . Solid lines are linear fitting.

molecule (1 mmol/L immersion concentration). It is found that a larger temperature difference brings significantly higher ΔV , which could be further demonstrated in the distribution histograms of the individual traces (right panel of Figure 1C). To quantitatively determine the Seebeck coefficient, we constructed the distribution histograms of thermovoltage at different temperature differences (Figure 1D) from more than 1000 individual traces, and the most probable thermovoltage could be determined from the Gaussian fitting of the distribution. Because the fluctuation of the molecular junction configurations inevitably occurs during the measurement process, the thermoelectric voltage from different trapped molecular junctions might exhibit different distributions [11]. By fitting the slope of the most-probable thermovoltage value versus the temperature differences, the Seebeck coefficient could be determined to be $-18.05 \pm 1.64 \mu\text{V/K}$.

To investigate the role of packing density in SAMs, the Seebeck coefficient was measured for **F-DPP** with increasing packing densities through immersing the gold electrode into corresponding 0.01, 0.1, and 1.0 mmol/L molecule solutions. The previous work had revealed that molecular interaction in the SAMs could be controlled by modulating the concentration of solution during the assembling process [26]. The X-ray photoelectron spectroscopy (XPS) semiquantitative analysis was conducted to confirm chemical composition of molecular monolayer and its atomic ratio (Table S1) [34]. The results suggest that more molecules

existed on the gold sample under the immersion of the molecule solutions with increased concentration, based on the atomic concentration of the S2p peak signal (Figure S3), and the XPS analysis indeed had demonstrated the formation of Au–S bonds in the SAMs.

Besides, analytical electrochemistry was also used to quantitatively determine how much gold surface was covered with **F-DPP** molecules at different immersion concentrations, according to a method modified from a previously published work [35]. The gold electrode with molecules assembled on was used as a working electrode, and a cyclic voltammetry (CV) was performed in 2.5 mmol/L $K_3Fe(CN)_6/K_4Fe(CN)_6$ solution containing 0.1 mol/L KNO_3 as the supporting electrolyte with a sweep rate of 100 mV/s, and the potential was controlled between -0.2 and 0.6 V to avoid other redox reactions from assembled **F-DPP**. A typical CV at different immersion concentrations was obtained (Figure 2A), there are apparent redox peaks from $K_3Fe(CN)_6/K_4Fe(CN)_6$ in all cases. The current at the region with potential over redox peak was mainly controlled by reactants diffusion, and the diffusion areas could be obtained by applying the Cottrell equation [36] (see Figure S4 for the application of Cottrell equation in this work). The diffusion areas of the bare gold electrode (without molecules assembled) were determined to be 0.0051 cm^2 , while it decreased to 0.0036 cm^2 for molecule-assembled gold electrode with 1 mmol/L immersion concentration (Table 1). The diffusion areas could reflect the assembled-molecule-occupied electrode areas, because SAMs with higher packing density left fewer areas for redox reaction and diffusion. Finally, the SAM surface coverage fraction of assembled molecules with different immersion concentrations was obtained according to the diffusion area compared to bare gold (Table 1 and inset of Figure 2B), varying from 7.84% (0.01 mmol/L immersed **F-DPP**) to 29.41% (1 mmol/L immersed **F-DPP**). In addition, a micro thermal gravimetric analyzer (μ -TGA) [37] was also applied to determine their packing density differences (Figure S5). All these characterizations indeed proved that the packing density could be controlled by modulating the immersion concentration during the assembling process.

It is found that the Seebeck coefficients of a single **F-DPP** molecule at increasing packing densities are

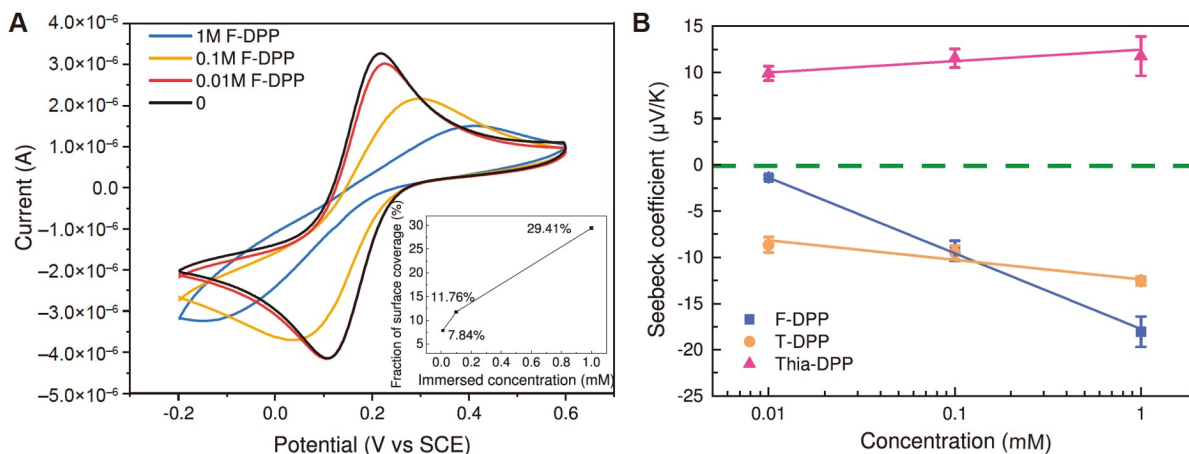


Figure 2 CV characterization on SAM surface coverage and Seebeck coefficient of three types of DPP. (A) CV measurements with **F-DPP** assembled gold as the working electrode at different immersion concentrations in 2.5 mmol/L $K_3Fe(CN)_6/K_4Fe(CN)_6$ containing 0.1 mol/L KNO_3 as the supporting electrolyte, standard calomel and Pt working as reference and counter electrode respectively. (Inset: surface coverage fraction of self-assembled **F-DPP** as a function of immersion concentration.) (B) Experimentally measured Seebeck coefficient value for **F-DPP** (blue squares), **T-DPP** (brown cycles) and **Thia-DPP** (magenta triangles). Error bars are the standard deviation in Gaussian fitting of thermoelectric voltages. The solid line indicates that the absolute Seebeck coefficient of the three DPPs increases with solution concentration. The green dashed line indicates that the Seebeck coefficient $S=0$.

Table 1 Immersion concentration-dependent surface coverage of **F-DPP** SAMs

Immersion concentration	CV analysis for SAM surface coverage	
	Diffusion area from Cottrell equation (cm ²)	SAM fraction of surface coverage (%)
0	0.0051	0
0.01 mmol/L	0.0047	7.84
0.1 mmol/L	0.0045	11.76
1 mmol/L	0.0036	29.41

-2.16 ± 0.29 $\mu\text{V/K}$ (0.01 mmol/L), -9.30 ± 1.08 $\mu\text{V/K}$ (0.1 mmol/L) and -18.05 ± 1.64 $\mu\text{V/K}$ (1 mmol/L) (Figure 2B and Table 2). These showed that the Seebeck coefficients of **F-DPP** maintain the same sign (negative) and increase dramatically with the increase of molecular packing density. More importantly, the Seebeck coefficient of the single-molecule junction could be enhanced near one order of magnitude, which is much larger than the mainstream tuning method called destructive quantum interference (DQI) with only two times enhancement up to now [20]. Furthermore, we observed a similar trend for **T-DPP** and **Thia-DPP**. The Seebeck coefficient of **T-DPP** varied from -8.65 ± 0.82 $\mu\text{V/K}$ (0.01 mmol/L) to -12.55 ± 0.47 $\mu\text{V/K}$ (1 mmol/L), and **Thia-DPP** varied from $+9.89 \pm 0.77$ $\mu\text{V/K}$ (0.01 mmol/L) to $+11.76 \pm 2.12$ $\mu\text{V/K}$ (1 mmol/L) (see Figures S6–S8 for details of conductance and Seebeck coefficient measurement). Interestingly, the sign of the Seebeck coefficient of **Thia-DPP** is opposite to **F-DPP** and **T-DPP**, meaning that altering the adjacent aromatic rings of the DPP core can influence the dominant frontier orbital of charge transport through the molecules. The negative Seebeck coefficient suggested that the Fermi levels (E_F) of **F-DPP** and **T-DPP** are closer to the lowest unoccupied molecular orbital (LUMO) level, and the transport is electron-dominated; the positive Seebeck coefficient suggested that the E_F of **Thia-DPP** is closer to the HOMO level, and transport is hole-dominated [38]. This trend is the same as that observed in oxidized oligothiophenes derivatives, in which the dominant charge carriers changed from holes to electrons with increasing molecular length [16].

To elucidate the origin of the experimentally observed trends, we investigated the transport properties of **F-DPP**, **T-DPP** and **Thia-DPP** junctions connected to the gold source and drain electrodes via $-\text{SMe}$ groups as shown in Figure 3A–3C (see more binding configurations for **F-DPP**, **T-DPP** and **Thia-DPP** in Figures S9 and S10) using DFT combined quantum transport theory. The material-specific mean-field Hamiltonian of each geometry obtained from SIESTA [39] was combined with quantum transport code Gollum [40] to obtain the electronic transmission coefficient, which controls electrical and thermoelectric properties.

To investigate the dependence of conductance and Seebeck coefficients on the packing density, we calculated the transport properties for junctions containing either a single-molecule (i.e., a monomer junction) or in the presence of two nearby molecules (i.e., optimized geometry of trimer junction is shown in Figure 3A–

Table 2 Single-molecule Seebeck coefficient and conductance measurements

Compounds with different immersion concentration	Seebeck coefficient ($\mu\text{V/K}$)	Measured conductance ($\log(G/G_0)$)
0.01 mmol/L F-DPP	-2.16 ± 0.29	-4.03
0.1 mmol/L F-DPP	-9.30 ± 1.08	-4.00
1 mmol/L F-DPP	-18.05 ± 1.64	-3.93
0.01 mmol/L T-DPP	-8.65 ± 0.82	-4.44
0.1 mmol/L T-DPP	-9.47 ± 0.74	-4.39
1 mmol/L T-DPP	-12.55 ± 0.47	-4.21
0.01 mmol/L Thia-DPP	$+9.89 \pm 0.77$	-4.52
0.1 mmol/L Thia-DPP	$+11.53 \pm 1.01$	-4.47
1 mmol/L Thia-DPP	$+11.76 \pm 2.12$	-4.41

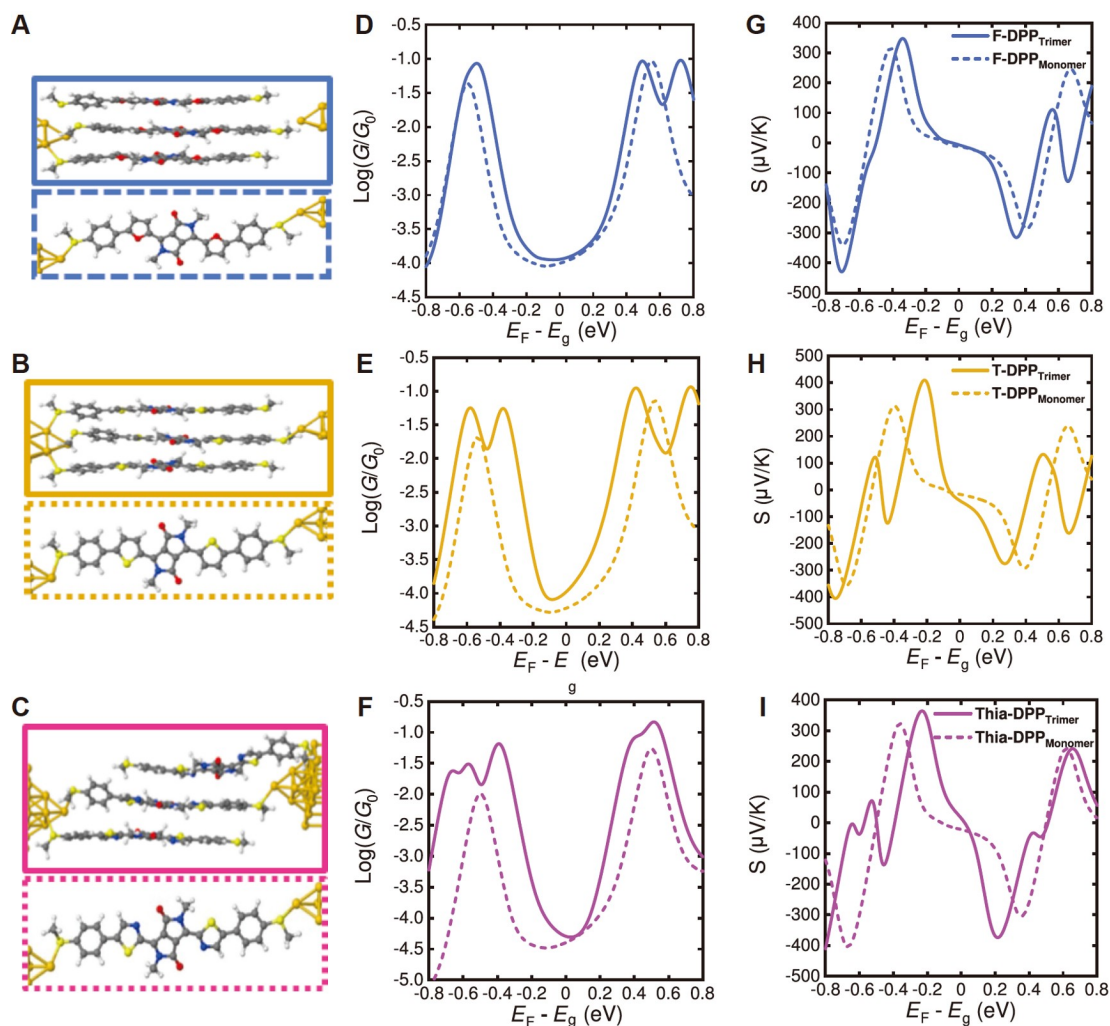


Figure 3 DFT calculated electrical and thermoelectric properties of the three DPP derivatives attached to gold electrodes via -SMe anchor groups, the distance between the central backbone and adjacent molecules is around 3.3 to 3.6 Å for **F-DPP**, **T-DPP** and **Thia-DPP** trimers. (A)–(C) Models for **F-DPP**, **T-DPP** and **Thia-DPP**, respectively. The solid line corresponds to three molecules in the junction (i.e., a trimer), and the dotted line corresponds to a single molecule in the junction (i.e., a monomer). (D)–(F) The calculated room-temperature electrical conductance of **F-DPP**, **T-DPP** and **Thia-DPP** as a function of the Fermi energy (E_F) relative to the mid-gap E_g . The solid lines represent trimers and dashed lines represent monomers. (G)–(I) The calculated room-temperature Seebeck coefficients of **F-DPP**, **T-DPP** and **Thia-DPP** as a function of Fermi energy (E_F) with the same shifting corresponding to conductance. The solid lines represent trimers and dashed lines represent monomers.

3C). We found that the trimer junctions have smaller highest occupied molecular orbital (HOMO)-LUMO gaps than monomers due to the splitting of HOMO and LUMO peaks caused by the interaction with nearby molecules [41]. The modelling demonstrates that the reduced HOMO-LUMO gap of the trimer generally increases the slope of transmission coefficients. Consequently, for a wide range of Fermi energies within the HOMO-LUMO gaps, the Seebeck coefficients of trimers are greater than or equal to monomers, and trimers have similar or higher conductance than the monomers (see Figures S11 and S12 for more details). These features are in qualitative agreement with the observed experimental trends (see Figures S5 and S6 for conductance measurements). DFT has difficulties in predicting the correct HOMO-LUMO gaps [42], charge transfer and Coulomb interaction for charged systems and particularly for these strong acceptor DPP-cores

[43,44]. On the other hand, the Fermi energy is located somewhere inside the HOMO-LUMO gap. Therefore, to compare results for monomer and trimer molecular junctions, we aligned their mid-gap of the conductance curve (Figure 3D–3F). The electrical conductance for **F-DPP** trimer (solid curve) and **F-DPP** monomer (dotted curve) remain in the same value (close to $10^{-4} G_0$), and those for **T-DPP**, **Thia-DPP** trimers and **T-DPP**, **Thia-DPP** monomers possess the conductance around 10^{-4} – $10^{-4.5} G_0$, which demonstrated a considerable consistency with the experimental data.

The corresponding Seebeck coefficients are displayed in Figure 3G–3I. In terms of the net Voronoi charge distribution shown in Table S2, the **Thia-DPP** molecule gains more electrons than **F-DPP** and **T-DPP**, which could induce more vital Coulomb interaction for the negatively charged molecule, moving the energy levels upwards and pushing the HOMO closer to the Fermi energy. Indeed, if the Fermi energy is slightly below the mid-gap position for **Thia-DPP**, then the sign of the Seebeck coefficient would be positive, as shown to the left of the crossing point ($S=0$ and $E_F=-0.3$ eV) in the Seebeck plot of Figure 3I, which also reveals a higher Seebeck coefficient for the trimer junctions. Conversely, for **F-DPP** and **T-DPP**, the right sides of the crossing point of $S=0$ have a negative Seebeck coefficient and greater magnitudes for the trimers (Figure 3G and 3H). Figure 3G–3I clearly shows that the Seebeck coefficient for the trimer junctions (solid lines) typically has a higher magnitude than the monomers (dotted lines), in agreement with the experimental trends.

DISCUSSION

In conclusion, we experimentally investigated the Seebeck coefficients of a series of single DPP derivatives varying the packing density of SAMs on the electrode surface using a modified STM-BJ technique. We discovered that the conductance channel of molecules could be changed from LUMO-dominated to HOMO-dominated by altering the adjacent aromatic rings of the DPP core. More importantly, the thermopower of molecular junctions could be enhanced by up to one order of magnitude via the increase of the packing density in SAMs. Combined DFT calculation revealed that the higher packing density leads to more substantial intermolecular coupling effects, which reduces the HOMO-LUMO gap and increases the Seebeck coefficient. Our results revealed that intermolecular coupling is of fundamental importance for designing highly efficient molecular thermoelectric devices and materials in the future.

MATERIALS AND METHODS

Materials

The target molecules were synthesized according to the previous reports [45–47]. For more details, see Figure S1. To obtain SAMs of different packing densities, the gold substrates, which are prepared by coating 200 nm Au film on silicon wafers, were immersed into 0.01, 0.1, 1 mmol/L molecule solution using the solvent of 1,2,4-trichlorobenzene (TCB, 99.9%, Sigma Aldrich) for 4 h. After that, the surface of the gold substrates with the assembled monolayer was rinsed by TCB and dried with N_2 gas.

Single-molecule conductance and Seebeck coefficient measurement

The single-molecule conductance and Seebeck coefficient measurements were performed using the home-built STM-BJ technique as described in previous reports [31]. The temperature was modulated by proportion integral differential (PID) control. Single-molecule junctions were fabricated following the electrical conductance measurement [48]. Once the conductance plateau was determined, the tip would be hovered and the tip/substrate distance fixed, followed by cutting off the bias voltage and the current amplifier. Instead, the voltage amplifier was connected to record the thermovoltage directly. After a period of time interval, the voltage amplifier would be cut off while the current amplifier is switched back to measure the conductance again. During the experiment, the tip withdrew from the sample until the tunneling current decreased to achieve the given threshold value. For further details, see Figure S2 in the Supplementary Information.

Computational methods

The optimized geometry and ground state Hamiltonian and overlap matrix elements of each structure were self-consistently obtained using the SIESTA implementation of DFT [39]. SIESTA employs norm-conserving pseudo-potentials to account for the core electrons and linear combinations of atomic orbitals to construct the valence states. The generalized gradient approximation (GGA) of the exchange and correlation functional is used with the Perdew-Burke-Ernzerh of parameterization (PBE), a double- ζ polarized (DZP) basis set, a real-space grid defined with an equivalent energy cut-off of 200 Ry [49]. The geometry optimization for each structure is performed to the forces smaller than 10 meV/Ang.

The mean-field Hamiltonian obtained from the converged DFT calculation was combined with our home-made implementation of the non-equilibrium Green's function method, Gollum [40], to calculate the phase-coherent, elastic scattering properties of each system consisting of left gold (source) and right gold (drain) leads and the scattering region (molecule **F-DPP**, **T-DPP** and **Thia-DPP**). The transmission coefficient $T(E)$ for electrons of energy E (passing from the source to the drain) is calculated via the relation:

$$T(E) = \text{Trace}(\Gamma_R(E)G^R(E)\Gamma_L(E)G^{R\dagger}(E)). \quad (1)$$

In this expression, $\Gamma_{L,R}(E) = i(\Sigma_{L,R}(E) - \Sigma_{L,R}^\dagger(E))$ describes the level broadening due to the coupling between left (L) and right (R) electrodes and the central scattering region, $\Sigma_{L,R}(E)$ are the retarded self-energies associated with this coupling and $G^R(E) = (ES - H - \Sigma_L - \Sigma_R)^{-1}$ is the retarded Green's function, where H is the Hamiltonian and S is the overlap matrix. Using the obtained transmission coefficient $T(E)$, the electrical conductance $G(T)$ and the Seebeck coefficient $S(T)$ can be calculated through the following formula:

$$G = G_0 L_0, \quad (2)$$

$$S = -\frac{L_0}{eTL_1}. \quad (3)$$

In the linear response, the quantity of Lorenz number $L_n(T, E_F)$ is given by

$$L_n(T, E_F) = \int_{-\infty}^{+\infty} dE (E - E_F)^n T(E), \quad (4)$$

where $G_0 = 2e^2/h$ is conductance quantum, e is the charge of a proton; h is the Planck's constant; E_F is the Fermi energy; $f(E) = (1 + \exp((E - E_F)/k_B T))^{-1}$ is the Fermi-Dirac distribution function, T is the temperature, and $k_B = 8.6 \times 10^{-5}$ eV/K is Boltzmann's constant.

Data availability

The original data are available from the corresponding authors upon reasonable request.

Acknowledgements

R.A. and Q.W. acknowledge the discussions with Dr. Iain Grace for the calculations. C.F., Q.C. and H.C. acknowledge Dr. Pengcheng Xu for the help of resonant microcantilever thermodynamic desorption characterization and Dr. Lina Chen for the help of X-ray photoelectron spectroscopy characterization.

Funding

This work was supported by the National Natural Science Foundation of China (21722305, 21933012, 31871877), the National Key R&D Program of China (2017YFA0204902), Natural Science Foundation of Fujian Province (2018J06004), Beijing National Laboratory for Molecular Sciences (BNLMS202010 and BNLMS202005), and the Fundamental Research Funds for the Central Universities (20720220020, 20720220072, 20720200068, 20720190002). The work in the UK was also supported by the Engineering and Physical Sciences Research Council (EPSRC, EP/M014452/1, EP/P027156/1, and EP/N03337X/1) by the European Commission, the Future and Emerging Technologies (FET) Open project 767187-QuIET and the European (EU) project Bac-to-Fuel.

Author contributions

W.H. conceived the concept. W.H., C.J.L. and Z.L. co-supervised the project. STM-BJ setup was constructed by H.C. and G.L. in W.H.'s group. H.C. and W.C. carried out single-molecule conductance and thermoelectric experiments. C.F. and H.C. analyzed the experimental data. R.A., Q.W. and S.H. performed theoretical simulations. Z.L. completed the synthesis of molecules used in this work. Y.G., H.Z., Y.Z., J.Z. and B.M. helped to analyze the data. C.F., Q.W., H.C., J. L., Z. L., C.J.L. and W.H. prepared the manuscript. All authors approved the final version of the manuscript.

Conflict of interest

The authors declare no conflict of interest.

Supplementary information

The supporting information is available online at <https://doi.org/10.1360/nso/20220039>. The supporting materials are published as submitted, without typesetting or editing. The responsibility for scientific accuracy and content remains entirely with the authors.

References

- 1 Wang Y, Yang L, Shi XL, *et al.* Flexible thermoelectric materials and generators: challenges and innovations. *Adv Mater* 2019; **31**: 1807916.
- 2 Xu K, Sun H, Ruoko TP, *et al.* Ground-state electron transfer in all-polymer donor-acceptor heterojunctions. *Nat Mater* 2020; **19**: 738–744.
- 3 Liang Z, Zhang Y, Souril M, *et al.* Influence of dopant size and electron affinity on the electrical conductivity and

- thermoelectric properties of a series of conjugated polymers. *J Mater Chem A* 2018; **6**: 16495–16505.
- 4 Zeng YJ, Wu D, Cao XH, *et al.* Nanoscale organic thermoelectric materials: measurement, theoretical models, and optimization strategies. *Adv Funct Mater* 2020; **30**: 1903873.
 - 5 Kim HS, Liu W, Chen G, *et al.* Relationship between thermoelectric figure of merit and energy conversion efficiency. *Proc Natl Acad Sci USA* 2015; **112**: 8205–8210.
 - 6 Shuai Z, Geng H, Xu W, *et al.* From charge transport parameters to charge mobility in organic semiconductors through multiscale simulation. *Chem Soc Rev* 2014; **43**: 2662.
 - 7 Zhang Q, Sun Y, Xu W, *et al.* Organic thermoelectric materials: Emerging green energy materials converting heat to electricity directly and efficiently. *Adv Mater* 2014; **26**: 6829–6851.
 - 8 Huang D, Yao H, Cui Y, *et al.* Conjugated-backbone effect of organic small molecules for n-type thermoelectric materials with ZT over 0.2. *J Am Chem Soc* 2017; **139**: 13013–13023.
 - 9 Russ B, Glaudell A, Urban JJ, *et al.* Organic thermoelectric materials for energy harvesting and temperature control. *Nat Rev Mater* 2016; **1**: 16050.
 - 10 Cao XH, Zhou WX, Chen CY, *et al.* Excellent thermoelectric properties induced by different contact geometries in phenalenyl-based single-molecule devices. *Sci Rep* 2017; **7**: 10842.
 - 11 Reddy P, Jang SY, Segalman RA, *et al.* Thermoelectricity in molecular junctions. *Science* 2007; **315**: 1568–1571.
 - 12 Kiršanskas G, Li Q, Flensburg K, *et al.* Designing π -stacked molecular structures to control heat transport through molecular junctions. *Appl Phys Lett* 2014; **105**: 233102.
 - 13 Finch CM, García-Suárez VM, Lambert CJ. Giant thermopower and figure of merit in single-molecule devices. *Phys Rev B* 2009; **79**: 033405.
 - 14 Zeier WG, Zevalkink A, Gibbs ZM, *et al.* Thinking like a chemist: Intuition in thermoelectric materials. *Angew Chem Int Ed* 2016; **55**: 6826–6841.
 - 15 Li Y, Xiang L, Palma JL, *et al.* Thermoelectric effect and its dependence on molecular length and sequence in single DNA molecules. *Nat Commun* 2016; **7**: 11294.
 - 16 Dell EJ, Capozzi B, Xia J, *et al.* Molecular length dictates the nature of charge carriers in single-molecule junctions of oxidized oligothiophenes. *Nat Chem* 2015; **7**: 209–214.
 - 17 Gehring P, Thijssen JM, van der Zant HSJ. Single-molecule quantum-transport phenomena in break junctions. *Nat Rev Phys* 2019; **1**: 381–396.
 - 18 Aiba A, Demir F, Kaneko S, *et al.* Controlling the thermoelectric effect by mechanical manipulation of the electron's quantum phase in atomic junctions. *Sci Rep* 2017; **7**: 7949.
 - 19 Garner MH, Koerstz M, Jensen JH, *et al.* Substituent control of σ -interference effects in the transmission of saturated molecules. *ACS Phys Chem Au* 2022; **2**: 282–288.
 - 20 Miao R, Xu H, Skripnik M, *et al.* Influence of quantum interference on the thermoelectric properties of molecular junctions. *Nano Lett* 2018; **18**: 5666–5672.
 - 21 Yee SK, Malen JA, Majumdar A, *et al.* Thermoelectricity in fullerene-metal heterojunctions. *Nano Lett* 2011; **11**: 4089–4094.
 - 22 Widawsky JR, Darancet P, Neaton JB, *et al.* Simultaneous determination of conductance and thermopower of single molecule junctions. *Nano Lett* 2012; **12**: 354–358.
 - 23 Baheti K, Malen JA, Doak P, *et al.* Probing the chemistry of molecular heterojunctions using thermoelectricity. *Nano Lett* 2008; **8**: 715–719.
 - 24 Li X, Wu Q, Bai J, *et al.* Structure-independent conductance of thiophene-based single-stacking junctions. *Angew Chem Int Ed* 2020; **59**: 3280–3286.
 - 25 Evangeli C, Gillemot K, Leary E, *et al.* Engineering the thermopower of C₆₀ molecular junctions. *Nano Lett* 2013; **13**: 2141–2145.
 - 26 Imahori H, Hasobe T, Yamada H, *et al.* Concentration effects of porphyrin monolayers on the structure and photoelectrochemical properties of mixed self-assembled monolayers of porphyrin and alkanethiol on gold electrodes.

- Langmuir* 2001; **17**: 4925–4931.
- 27 Nerngchamnong N, Yuan L, Qi DC, *et al.* The role of van der Waals forces in the performance of molecular diodes. *Nat Nanotech* 2013; **8**: 113–118.
- 28 Romaner L, Heimel G, Zojer E. Electronic structure of thiol-bonded self-assembled monolayers: Impact of coverage. *Phys Rev B* 2008; **77**: 045113.
- 29 Song H, Lee H, Lee T. Intermolecular chain-to-chain tunneling in metal-alkanethiol-metal junctions. *J Am Chem Soc* 2007; **129**: 3806–3807.
- 30 Jalal Uddin M, Khalid Hossain M, Hossain MI, *et al.* Modeling of self-assembled monolayers (SAMs) of Octadecanethiol and Hexadecanethiol on gold (Au) and silver (Ag). *Results Phys* 2017; **7**: 2289–2295.
- 31 Chen H, Sangtarash S, Li G, *et al.* Exploring the thermoelectric properties of oligo(phenylene-ethynylene) derivatives. *Nanoscale* 2020; **12**: 15150–15156.
- 32 Xu B, Tao NJ. Measurement of single-molecule resistance by repeated formation of molecular junctions. *Science* 2003; **301**: 1221–1223.
- 33 Shi L, Majumdar A. Thermal transport mechanisms at nanoscale point contacts. *J Heat Transfer* 2001; **124**: 329–337.
- 34 Grant JT. Methods for quantitative analysis in XPS and AES. *Surf Interface Anal* 1989; **14**: 271–283.
- 35 Suroviev A. Determining surface coverage of self-assembled monolayers on gold electrodes. *Chem Educator*, 2012; **17**: 83.
- 36 Heinze J, Bard AJ, Faulkner LF. *Electrochemical Methods-Fundamentals and Applications*. New York: John Wiley & Sons, Ltd., 1981.
- 37 Yu H, Li X, Gan X, *et al.* Resonant-cantilever bio/chemical sensors with an integrated heater for both resonance exciting optimization and sensing repeatability enhancement. *J Micromech Microeng* 2009; **19**: 045023.
- 38 Paulsson M, Datta S. Thermoelectric effect in molecular electronics. *Phys Rev B* 2003; **67**: 241403.
- 39 Soler JM, Artacho E, Gale JD, *et al.* The SIESTA method for *ab initio* order-*n* materials simulation. *J Phys-Condens Matter* 2002; **14**: 2745–2779.
- 40 Ferrer J, Lambert CJ, García-Suárez VM, *et al.* Gollum: A next-generation simulation tool for electron, thermal and spin transport. *New J Phys* 2014; **16**: 093029.
- 41 Kashimoto Y, Yonezawa K, Meissner M, *et al.* The evolution of intermolecular energy bands of occupied and unoccupied molecular states in organic thin films. *J Phys Chem C* 2018; **122**: 12090–12097.
- 42 Lambert CJ. Basic concepts of quantum interference and electron transport in single-molecule electronics. *Chem Soc Rev* 2015; **44**: 875–888.
- 43 Wang X, Jiang B, Du C, *et al.* Fluorinated dithienyl-diketopyrrolopyrrole: a new building block for organic optoelectronic materials. *New J Chem* 2019; **43**: 16411–16420.
- 44 Neaton JB, Hybertsen MS, Louie SG. Renormalization of molecular electronic levels at metal-molecule interfaces. *Phys Rev Lett* 2006; **97**: 216405.
- 45 Mueller CJ, Singh CR, Fried M, *et al.* High bulk electron mobility diketopyrrolopyrrole copolymers with perfluorothiophene. *Adv Funct Mater* 2015; **25**: 2725–2736.
- 46 Sonar P, Zhuo JM, Zhao LH, *et al.* Furan substituted diketopyrrolopyrrole and thienylenevinylene based low band gap copolymer for high mobility organic thin film transistors. *J Mater Chem* 2012; **22**: 17284.
- 47 Carsten B, Szarko JM, Lu L, *et al.* Mediating solar cell performance by controlling the internal dipole change in organic photovoltaic polymers. *Macromolecules* 2012; **45**: 6390–6395.
- 48 Haiss W, van Zalinge H, Higgins SJ, *et al.* Redox state dependence of single molecule conductivity. *J Am Chem Soc* 2003; **125**: 15294–15295.
- 49 Perdew JP, Burke K, Ernzerhof M. Perdew, burke, and ernzerhof reply. *Phys Rev Lett* 1998; **80**: 891.